RSC Advances

PAPER

View Article Online
View Journal | View Issue

Open Access Article. Published on 24 March 2016. Downloaded on 12/4/2025 5:50:39 AM.
This article is licensed under a Creative Commons Attribution-NonCommercial 3.0 Unported Licence.

Cite this: *RSC Adv.*, 2016, **6**, 34674

Structural and magnetic properties of heptacoordinated Mn^{II} complexes containing a 15-membered pyridine-based macrocycle and halido/pseudohalido axial coligands†

Bohuslav Drahoš, Radovan Herchel and Zdeněk Trávníček*

A series of heptacoordinated Mn^{II} compounds with a pentadentate 15-membered pyridine-based macrocycle 15-pyN_3O_2(3,12,18-triaza-6,9-dioxabicyclo[12.3.1]octadeca-1(18),14,16-triene) and two axially coordinated halido/pseudohalido coligands (X), having a monomeric $[Mn(15\text{-}pyN_3O_2)X_2]$ (X = Br^- (**1**), I^- (**2**), N_3^- (**3**), NCS^- (**4**)) or polymeric $\{[Mn(15\text{-}pyN_3O_2)X](ClO_4)\}_n$ (X = CN^- (**5**)) composition, was prepared and thoroughly characterized. Single crystal X-ray analysis of **2**, **3** and **4** determined the distorted pentagonal-bipyramidal geometry of the complexes. The analysis of the magnetic data of complexes **1**–**4** revealed non-zero values of the axial zero-field splitting parameter D ($|D| < 0.7$ cm^{-1}) and weak antiferromagnetic intermolecular interactions (molecular field correction parameter $zj \approx -0.1$ cm^{-1}). As for the 1D polymeric complex **5**, a small antiferromagnetic exchange coupling was found between Mn^{II} centres, with $J = -1.72$ cm^{-1}. The experimentally obtained magnetic parameters (J or zj) were compared with those theoretically calculated at the DFT level in order to reveal the magnetic exchange pathways in **2**–**4** and to support the polymeric structure of **5** ($J^{EXP} = -2.79$ cm^{-1} *vs.* $J^R/J^Y = -2.54/-3.06$ cm^{-1}, when the dinuclear spin Hamiltonian was used). It has been also found that extensive systems of hydrogen bonds, non-covalent contacts and π–π stacking interactions present in the crystal structures of **2**, **3** and **4** have an impact on the formation of supramolecular 1D chains, and as a consequence of this on the magnetic properties of the complexes. Contrary to non-covalent contacts, the influence of the axial ligands on the magnetic nature of the complexes seems to be negligible.

Received 10th February 2016
Accepted 16th March 2016

DOI: 10.1039/c6ra03754b

www.rsc.org/advances

Introduction

Despite a long history of chemistry of 15-membered pyridine-based macrocycles with five donor atoms, which date from the 1960s and have been recently reviewed,[1,2] these macrocyclic ligands (mainly those with five nitrogen or three nitrogen and two oxygen donor atoms) still attain strong interest of coordination chemists and magnetochemists as well as theoreticians due to their application potential in molecular magnetism, various types of sensors, and spintronics.[3] Among this rather extensive group of compounds, our attention has been mainly focused on the 15-membered macrocycles with a pyridine moiety incorporated into the macrocyclic ligand scaffold and two oxygen and two secondary nitrogen atoms (15-pyN_3O_2 = **L** in Fig. 1). The synthesis of 15-pyN_3O_2 is well known[4] and it is based on the cyclization of pyridine-2,6-dicarbaldehyde with 1,8-diamino-3,6-dioxaoctane using Mn^{II} as a template providing a macrocyclic Schiff base followed by reduction with $NaBH_4$.[4] The structural, magnetic and redox properties of the selected transition metal complexes containing 15-pyN_3O_2 and chlorido coligand(s), *i.e.* $[M^{II}\mathbf{L}Cl_2]$ where M = Mn, Co, Ni, Zn, $[Fe^{III}\mathbf{L}Cl_2]Cl$ and $[Cu^{II}\mathbf{L}Cl]Cl$, were described recently.[5] The coordination number of 7 was found in $[M\mathbf{L}Cl_2]^{0/+}$ (M = Mn^{II}, Fe^{III}, Co^{II}) and 5 + 2 in $[Ni^{II}\mathbf{L}Cl_2]$, where the two chlorido ligands occupied two axial positions in the pentagonal bipyramid, whereas the tetragonal-pyramidal coordination environment in $[Cu^{II}\mathbf{L}Cl]Cl$ and $[Zn^{II}\mathbf{L}Cl_2]$ corresponded to the coordination number of 4 + 1 and 5, respectively.[5] All metals in the above-mentioned complexes were in high-spin (HS) states, with $S = 5/2$ for Mn^{II} and Fe^{III}, $S = 3/2$ for Co^{II}, $S = 1$ for Ni^{II}, and $S = 1/2$ for Cu^{II}. Moreover, a large axial anisotropy was found for Co^{II} and Ni^{II} complexes, with $D(Co) \approx 40$ cm^{-1}, and $D(Ni) \approx -6.0$ cm^{-1}.[5]

Many Mn^{II} complexes with the structurally similar Schiff base ligand 15-$pydienN_3O_2$ (Fig. 1) were studied previously. For example, the $[Mn(15\text{-}pydienN_3O_2)(NCS)_2]$[6] complex with two

Department of Inorganic Chemistry & Regional Centre of Advanced Technologies and Materials, Faculty of Science, Palacký University, 17. listopadu 12, CZ-771 46 Olomouc, Czech Republic. E-mail: zdenek.travnicek@upol.cz; Fax: +420 585634954; Tel: +420 585634352

† Electronic supplementary information (ESI) available: Comparison of IR spectra of the complexes **1**–**5**, TG/DTA results for complex **4**, additional X-ray diffraction analysis data (for complexes **2**, **3** and **4**) and magnetic data for the complexes **1**–**5**. CCDC 1442331–1442333. For ESI and crystallographic data in CIF or other electronic format see DOI: 10.1039/c6ra03754b

This journal is © The Royal Society of Chemistry 2016

Open Access Article. Published on 24 March 2016. Downloaded on 12/4/2025 5:50:39 AM.
This article is licensed under a Creative Commons Attribution-NonCommercial 3.0 Unported Licence.

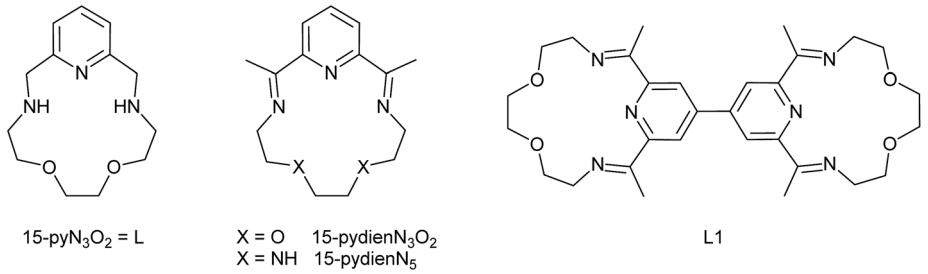

Fig. 1 Structural formulas of the studied ligand (15-pyN$_3$O$_2$ = **L**) and other ligands discussed in the text.

isothiocyanato ligands coordinated in axial positions of the pentagonal-bipyramid was described. Indeed, the [Mn(15-pydienN$_3$O$_2$)]$^{2+}$ complex unit has been usually coupled into heteronuclear oligomers of polymeric complexes with different cyanidometallates $[M^{I}(CN)_2]^-$,[7] $[M^{II}(CN)_4]^{2-}$,[8] or $[M^{III}(CN)_6]^{3-}$,[8,9] (M^{I} = Ag, Au; M^{II} = Ni, Pd, Pt; M^{III} = Fe, Cr, Co), showing antiferromagnetic exchange interactions between Mn^{II} and Cr^{III} [8] or ferromagnetic exchange interactions between Mn^{II} and Fe^{III}.[9] Furthermore, other bridging units like azido[10] or dicyanamido[11] ligands were used to link the Mn^{II} complex of the pentaaza Schiff base analogue 15-pydienN$_5$ (Fig. 1), forming a similar polymeric 1D chain with antiferromagnetic exchange coupling between adjacent Mn^{II} centres ($J = -4.8$ cm^{-1} for azide,[10] $J = -0.49$ cm^{-1} for dicyanamide).[11] Additionally, the Mn^{II} complex of the bimacrocyclic ligand **L1** (Fig. 1) [Mn$_2$(**L1**)Cl$_2$(H$_2$O)$_2$]Cl$_2$ revealed a very weak antiferromagnetic intradimer coupling ($J_{ex} = -0.51$ K) between the two Mn^{II} metal centres in the dimeric unit.[12] Nevertheless, the influence of the ligands in axial positions (X) in mononuclear heptacoordinated complexes of the general composition [MLX$_2$] (M = manganese or other transition metals, **L** = a pentadentate pyridine-based macrocyclic ligand) on the magnetic properties of these complexes has not been systematically studied. On the other hand, Mn^{II} complexes showing other interesting magnetic properties, *e.g.* spin crossover (spin transition induced by external stimuli, usually by changing temperature or upon light irradiation), are very rare. The known examples including Prussian blue analogue $Rb^{I}Mn^{II}[Fe^{III}(CN)_6]$, manganocene derivatives (η^5-C$_5$H$_4$R)$_2$Mn (with R = H, Me, Et), or complexes with nitrosyl and dibenzotetramethyltetraaza[14]annulene (tmtaa), [(tmtaa)Mn{NO}]·THF, were already reviewed in the literature.[13]

As has been shown previously for many examples of transition metal complexes with Schiff bases,[14–16] the magnetic properties, especially the spin transition (spin crossover),[13] single molecule magnet (SMM)[17] behaviour, or magnetic anisotropy also for the 3d^5 configuration,[18,19] can be tuned by substitution of the small coligands providing a different ligand field which has an impact on the electronic structure of such systems. Such a strategy has been employed in this work in order to reveal the influence of the axial ligands on the crystal structure, on the system of non-covalent contacts and consequently on the magnetic properties. Therefore a series of Mn^{II} complexes with macrocyclic ligand 15-pyN$_3$O$_2$ and various coligands (*i.e.* Br^- (**1**), I^- (**2**), N_3^- (**3**), SCN^- (**4**) and CN^- (**5**)) is studied. The synthesis and thorough characterization of the prepared compounds by different techniques is described. The X-ray structures of the complexes with two I^- (**2**), N_3^- (**3**) and SCN^- (**4**) coligands are described in detail. The variable-temperature and variable-field magnetization measurements, which were performed for all the compounds, are discussed in order to reveal the magnetic properties of the complexes, such as magnetic anisotropy and magnetic exchange interactions. The results following from the magnetic data are supported by DFT calculations which helped us to identify the magnetic exchange pathways. This is the first example of a systematic investigation of pentagonal bipyramidal Mn^{II} complexes where the influence of the axial ligands is studied simultaneously by comparing the molecular structures, temperature/field-dependent magnetic data and DFT calculations.

Experimental

Synthesis

The ligand 15-pyN$_3$O$_2$ = **L** (3,12,18-triaza-6,9-dioxabicyclo[12.3.1]octadeca-1(18),14,16-triene) was synthesized according to the previously described literature procedure.[4] All other chemicals and solvents were purchased from commercial sources (Across Organics, Geel, Belgium and Sigma Aldrich, St. Louis, MO, USA and Penta, Prague, Czech Republic) and used as received.

[MnLBr$_2$] (1). **L** (100 mg, 0.40 mmol) and MnBr$_2$·4H$_2$O (114 mg, 0.40 mmol) were dissolved in 5 mL of methanol (MeOH) at room temperature. The obtained yellow solution was filtered through a Millipore syringe filter (0.45 μm) and the filtrate was left to a vapour diffusion of diethyl ether (Et$_2$O) at 5 °C. After several days, crystals of the desired complex were formed. They were collected by filtration on a glass frit and dried open to air at room temperature. The product was obtained in the form of pale yellow crystals (127 mg, yield 68.6%).

MS *m*/*z* (+): 385.21 [Mn**L**Br]$^+$. Anal. calcd (%) for C$_{13}$H$_{21}$N$_3$O$_2$MnBr$_2$: C, 33.50; H, 4.54; N, 9.02. Found: C, 33.54; H, 4.75; N, 8.59.

[MnLI$_2$] (2). **L** (100 mg, 0.40 mmol) and Mn(ClO$_4$)$_2$·6H$_2$O (144 mg, 0.40 mmol) were dissolved in 3 mL of MeOH at room temperature. NH$_4$I (173 mg, 1.20 mmol, 3 eqv.) was dissolved in a 10 mL vial in 2.5 mL of MeOH, and this solution was added to the solution of the Mn^{II} complex prepared in the first step. The

Open Access Article. Published on 24 March 2016. Downloaded on 12/4/2025 5:50:39 AM. This article is licensed under a Creative Commons Attribution-NonCommercial 3.0 Unported Licence.

yellow solution obtained was filtered through a Millipore syringe filter (0.45 μm) and the filtrate was left to a vapour diffusion of Et_2O at 5 °C. After several days, well-shaped crystals of the complex were formed. They were collected by filtration on a glass frit and dried open to air at room temperature. The product was obtained as yellow needle-shaped crystals (148 mg, yield 66.4%).

MS *m/z* (+): 433.17 $[MnLI]^+$. Anal. calcd (%) for $C_{13}H_{21}N_3O_2MnI_2$: C, 27.88; H, 3.78; N, 7.50. Found: C, 28.21; H, 3.85; N, 7.40.

[MnL(N$_3$)$_2$] (3). **L** (100 mg, 0.40 mmol) and $Mn(OAc)_2 \cdot 6H_2O$ (101 mg, 0.40 mmol) were dissolved in a 25 mL dropping flask in 5 mL of MeOH at room temperature. A suspension of NaN_3 (65 mg, 1.00 mmol, 2.5 eqv.) in 2.5 mL of MeOH was added. The obtained mixture was heated to reflux and a clear yellow solution was formed. The hot solution was filtered through a Millipore syringe filter (0.45 μm) and the filtrate was left to a vapour diffusion of Et_2O at 5 °C. After several days, well-shaped crystals of the complex were formed, collected by filtration on a glass frit and dried open to air at room temperature. The product was obtained in the form of yellow-brown block-shaped crystals (98 mg, yield 63.2%).

MS *m/z* (+): 347.96 $[MnL(N_3)]^+$. Anal. calcd (%) for $C_{13}H_{21}N_9O_2Mn$: C, 40.00; H, 5.42; N, 32.30. Found: C, 39.60; H, 5.19; N, 32.77.

[MnL(NCS)$_2$] (4). **L** (100 mg, 0.40 mmol) and $MnCl_2 \cdot 4H_2O$ (79 mg, 0.40 mmol) were dissolved in 4 mL of MeOH at room temperature. To this yellow solution, NH_4SCN (151 mg, 2.00 mmol, 5 eqv.) dissolved in 2 mL of MeOH was added. After the mixing of both solutions, a white crystalline precipitate was formed and filtrated under reduced pressure on a glass frit, washed twice with 2 mL of MeOH and twice with 4 mL of Et_2O and dried open to air at room temperature. The obtained pale yellow crude product (139 mg) was recrystallized from a hot MeOH/water mixture. The pure product was isolated in the form of yellow block-shaped crystals (96 mg, yield 57.1%).

MS *m/z* (+): 364.22 $[MnL(SCN)]^+$. Anal. calcd (%) for $C_{15}H_{21}N_5O_2S_2Mn$: C, 42.65; H, 5.01; N, 16.58; S, 15.18. Found: C, 42.78; H, 5.02; N, 16.27; S 15.52.

{[MnL(μ-CN)](ClO$_4$)}$_n$ (5). **L** (100 mg, 0.40 mmol) and $Mn(ClO_4)_2 \cdot 6H_2O$ (144 mg, 0.40 mmol) were dissolved in 3 mL of MeOH at room temperature. A solution of NaCN (49 mg, 1 mmol, 2.5 eqv.) in 2.5 mL of MeOH was added and a white precipitate immediately formed. A small amount of ascorbic acid (6 mg, 0.04 mmol) was added to prevent the oxidation of Mn^{II} by air. The suspension was heated to reflux and an additional 2 mL of MeOH was added, but the precipitate did not dissolve. After 10 minutes of reflux, the suspension was cooled down to room temperature. The yellow precipitate was filtered under reduced pressure on a glass frit, washed with 2 mL of MeOH and twice with 2 mL of Et_2O and dried open to air at room temperature. The product was obtained as a yellow powder (129 mg, yield 75.0%).

MS *m/z* (+): 332.06 $[MnL(CN)]^+$, 405.10 $[MnL(ClO_4)]^+$. Anal. calcd (%) for $C_{14}H_{21}N_4O_6ClMn$: C, 38.95; H, 4.90; N, 12.98. Found: C, 38.88; H, 5.01; N, 12.99.

Physical methods

Measurement of elemental analysis (C, H, N) was carried out using a Flash 2000 CHNO-S Analyzer (Thermo Scientific, Waltham, MA, USA). Mass spectrometry (MS) was recorded on a LCQ Fleet Ion Mass Trap mass spectrometer (Thermo Scientific, Waltham, MA, USA) equipped with an electrospray ion source and 3D ion-trap detector in the positive mode. Infrared (IR) spectra of the complexes were collected on a Thermo Nicolet NEXUS 670 FT-IR spectrometer (Thermo Nicolet, Waltham, MA, USA) employing the ATR technique on a diamond plate in the range of 400–4000 cm^{-1}. Simultaneous thermogravimetric (TG) analysis and differential thermal analysis (DTA) were performed on a Exstar TG/DTA 6200 thermal analyzer (Seiko Instruments Inc., Torrance, CA, USA) with a dynamic air atmosphere (100 mL min^{-1}) in the temperature interval of 25–900 °C with a heating rate of 5.0 °C min^{-1}. The magnetic data were measured on powder samples using a SQUID magnetometer MPMS-XL7 (Quantum Design) for **1** and a PPMS Dynacool system (Quantum Design) with the VSM option for **2–5**. The experimental data were corrected for the diamagnetism and signal of the sample holder. The X-ray powder diffraction pattern for complex **1** was recorded on a MiniFlex600 (Rigaku) instrument equipped with the Bragg–Brentano geometry and iron-filtered Cu K$\alpha_{1,2}$ radiation.

X-ray diffraction analysis

Single crystals of complexes **2**, **3** and **4** suitable for X-ray structure analysis were prepared by vapour diffusion of Et_2O into a MeOH solution of the appropriate complex at 5 °C. Moreover, some other recrystallization or diffusion experiments were performed in the case of complexes **1** and **5**, but suitable single crystals were not prepared. X-ray diffraction data of **2** and **4** were collected with a Rigaku HighFlux HomeLab™ universal dual wavelength (Mo Kα and Cu Kα) single crystal diffractometer at 120(2) K, while the Mo Kα radiation (λ = 0.71075 Å) was used to obtain the diffraction data. The diffractometer was equipped with the Eulerian 3 circle goniometer and the Rigaku Saturn724+ (2 × 2 bin mode) detector. Data reduction and correction of the absorption effect were performed using the XDS software package.[20] The X-ray diffraction data of **3** were collected on a Bruker D8 QUEST diffractometer equipped with a PHOTON 100 CMOS detector using Mo Kα radiation. The APEX3 software package[21] was used for data collection and reduction of **3**. The molecular structures of **2–4** were solved by direct methods and refined by the full-matrix least-squares procedure SHELXL (version 2014/7).[22] Hydrogen atoms of all the structures were found in the difference Fourier maps and refined (except for N-attached H atoms) using a riding model, with C–H = 0.95 $(CH)_{ar}$ and C–H = 0.99 (CH_2) Å, and with $U_{iso}(H) = 1.2U_{eq}$ (CH, CH_2, NH). The highest peak of 5.82 e Å^{-3} is located 1.61 Å from I1b in **2**, while the peak of 4.01 e Å^{-3} is located 0.82 Å from Mn1b in **4**. The molecular and crystal structures of all the studied complexes, depicted in Fig. 2 and 3, respectively, were drawn using the Mercury software.[23]

 This journal is © The Royal Society of Chemistry 2016

Open Access Article. Published on 24 March 2016. Downloaded on 12/4/2025 5:50:39 AM.
This article is licensed under a Creative Commons Attribution-NonCommercial 3.0 Unported Licence.

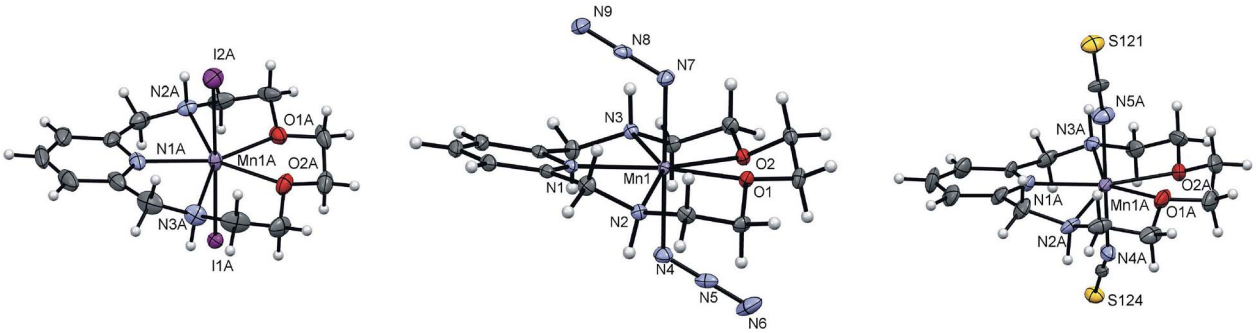

Fig. 2 Molecular structures of [MnLI$_2$] (**2**) (left), [MnL(N$_3$)$_2$] (**3**) (middle), and [MnL(NCS)$_2$] (**4**) (right). Non-hydrogen atoms are drawn as thermal ellipsoids at the 50% probability level. Only one of two (for **2**) and three (for **4**) crystallographically independent molecules are shown for clarity.

Computational details

The theoretical calculations were carried out with the ORCA 3.0.3 computational package.[24] The calculations of the isotropic exchange parameters J were done by the broken symmetry approach[25] using the hybrid B3LYP functional[26] and polarized triple-ζ quality basis set def2-TZVP(-f) proposed by Ahlrichs and coworkers for all atoms.[27] The calculations utilized the RI approximation with the decontracted auxiliary def2-TZV/J Coulomb fitting basis sets and the chain-of-spheres (RIJCOSX) approximation to exact exchange as implemented in ORCA.[28] Increased integration grids (Grid5 in ORCA convention) and tight SCF convergence criteria were used in all calculations. In all the cases the calculations were based on the experimentally determined X-ray molecular structures, but the all hydrogen atom positions were optimized using the B3LYP functional and atom pairwise dispersion correction to the DFT energy with Becke–Johnson damping (D3BJ).[29] In the case of the molecular fragment [(CN)Mn**L**(μ-CN)Mn**L**(CN)]$^+$ of **5**, the whole geometry was optimized using B3LYP/def2-TZVP(-f)+D3BJ. The spin densities were visualized with the program VESTA 3.[30]

Results and discussion

Synthesis

Previously, Mn^{II} complexes with **L** containing coordinated two chlorido coligands[5] or one chlorido coligand and one water molecule[4] were prepared by direct mixing of manganese(II) salt and **L**. This simple procedure was employed in the preparation of complex **1**, for which MnBr$_2$ was directly complexated by **L**.

complex	[Mn**L**Cl$_2$]^a	[Mn**L**I$_2$] (**2**)	[Mn**L**(N$_3$)$_2$] (**3**)	[Mn**L**(NCS)$_2$] (**4**)
	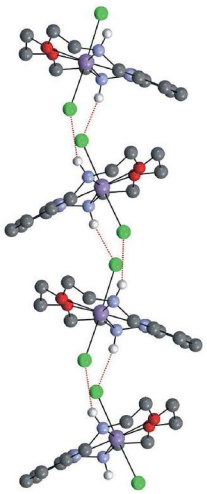	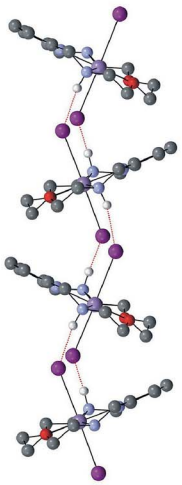	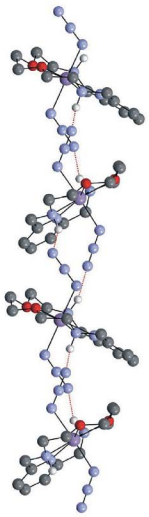	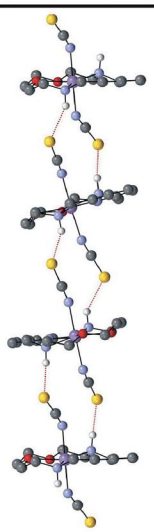
angle (°)	41.6	45.6	60.2	8.2, 13.5, 5.3
Mn···Mn (Å)	6.627(1)	7.337(2), 7.355(2)^b	7.655(1)	7.880(1), 8.024(1), 8.499(1)^b

Fig. 3 Part of the crystal structure of [MnLCl$_2$],[5] **2**, **3** and **4** showing the N–H···Cl, N–H···I, N–H···N, and N–H···S non-covalent contacts (red dashed lines), respectively, forming 1D chain supramolecular structures together with the values of angles between the MnN$_3$O$_2$ least-square planes and the Mn···Mn distances in the 1D chains. ^{a}Data adopted from ref. 5. ^{b}Two and three crystallographically independent molecules were found in the asymmetric unit of **2** and **4**, respectively.

Open Access Article. Published on 24 March 2016. Downloaded on 12/4/2025 5:50:39 AM.
This article is licensed under a Creative Commons Attribution-NonCommercial 3.0 Unported Licence.

During the synthesis of compounds **2–5**, various manganese(II) salts, with anions with a low coordination ability (*e.g.* perchlorate or acetate), were complexated by **L** in the first step forming the $[Mn\mathbf{L}]^{2+}$ complex unit, while an excess of the appropriate coligand in the form of sodium or ammonium salt was added in the second step, during which this anion was coordinated to the manganese(II) centre. These two steps were designed in such a way that the side products were well soluble in MeOH (*i.e.* NH_4ClO_4, NH_4Cl, CH_3CO_2Na or $NaClO_4$) and did not contaminate the product during its consequent crystallization induced by Et_2O vapour diffusion.

X-ray diffraction analysis

The molecular structures of the complexes **2**, **3** and **4** are similar (Tables 1 and 2, Fig. 2, Tables S1 and S2, Fig. S1 and S2†). The crystal structures of **2** and **4** involve two and three, respectively, crystallographically independent molecules in the asymmetric units. However, the data for one of those independent molecules are discussed in the main text and listed in Table 2 (full data sets are available in Table S1,† all independent molecules are shown in Fig. S1 and S2 in the ESI†).

In all the cases, the Mn^{II} central atom adopts pentagonal-bipyramidal geometry with the coordination number of 7 (Fig. 2). The pentadentate macrocycle **L** is coordinated in an equatorial pentagonal plane with the shortest $Mn–N_{py}$ distances ~2.10–2.20 Å in comparison with the $Mn–N_H$ distances, ranging from 2.27 to 2.33 Å, and the Mn–O distance ranging from 2.28 to 2.33 Å (Table 2). The two axial positions are occupied with two iodido ligands in **2**, for which the Mn–I distances are much longer (2.95 and 3.03 Å, Table 2) in comparison with the Mn–N and Mn–O distances providing elongation of the pentagonal-bipyramidal coordination sphere in the axial directions. This is in accordance with the larger ionic radius of the iodide anions. Consequently the Mn–I distances are also longer in comparison with the same complex with coordinated chlorido coligands described previously having Mn–Cl distances of 2.53 and 2.55 Å.[5]

On the other hand, in the case of coordination of two azido or thiocyanato ligands in **3** or **4**, the $M–N_{axial}$ distances are shorter than those to the macrocyclic donor atoms (Table 2) providing axial compression of the pentagonal-bipyramidal coordination sphere. A further interesting feature of complexes **3** (with N_3^-) and **4** (with NCS^-) is associated with the value of the Mn–N–N(C) angle, which is 119.6/121.2° for **3** indicating a similar coordination fashion of both azido ligands, and 145.7/165.0°, 141.1/142.9° or 165.1/149.1° for **4** (Table 3) pointing to a different coordination mode in each independent molecule found in the asymmetric unit, which shows that the coordination of NCS^- to the Mn^{II} centre is closer to linear in comparison with the N_3^- ligand. For **3**, the observed Mn–N–N angles are very similar to the value 118.8° found in the 1D chain structure of $([Mn(15\text{-pydien}N_5)(N_3)]^+)_n$.[10]

Table 1 Crystal data and structure refinements for the studied complexes

Compound	**2**	**3**	**4**
Formula	$C_{13}H_{21}I_2MnN_3O_2$	$C_{13}H_{21}MnN_9O_2$	$C_{15}H_{21}MnN_5O_2S_2$
M_r	560.07	390.33	422.43
Colour	Yellow	Orange	Pale brown
Temperature (K)	120(2)	120(2)	120(2)
Wavelength (Å)	0.71073	0.71073	0.71073
Crystal system	Monoclinic	Monoclinic	Triclinic
Space group	$P2_1/n$	$P2_1/n$	$P1$[a]
a (Å)	14.6223(10)	9.8283(6)	10.1382(7)
b (Å)	16.5304(12)	12.8416(7)	11.3567(8)
c (Å)	15.2077(11)	13.4703(9)	14.0782(10)
α (°)	90	90	103.348(2)
β (°)	98.7810(10)	100.300(2)	110.850(2)
γ (°)	90	90	101.570(2)
U (Å^3)	3632.8(4)	1672.70(18)	1400.79(17)
Z	8	4	3
D_{calc} (g cm^{-3})	2.048	1.550	1.502
μ (mm^{-1})	4.133	0.819	0.949
F (000)	2136	812	657
θ range for data collection (°)	1.800–24.998	2.375–27.173	1.640–25.000
Refl. collected	27 041	116 071	14 537
Independent refl.	6390	3720	8526
R (int)	0.0311	0.0554	0.0156
Data/restrains/parameters	6390/0/379	3720/0/226	8526/3/677
Completeness to θ (%)	99.8	100.0	98.1
Goodness-of-fit on F^2	1.093	1.088	1.057
$R1$, w$R2$ ($I > 2\sigma(I)$)	0.0641, 0.1746	0.0258, 0.0578	0.0676, 0.1737
$R1$, w$R2$ (all data)	0.0653, 0.1756	0.0330, 0.0608	0.0677, 0.1738
Largest diff. peak and hole (Å^{-3})	5.82 and −2.74	0.24 and −0.28	4.01 and −1.02
CCDC number	1442331	1442332	1442333

[a] The value of the Flack parameter is 0.54(3).

 This journal is © The Royal Society of Chemistry 2016

Open Access Article. Published on 24 March 2016. Downloaded on 12/4/2025 5:50:39 AM.
This article is licensed under a Creative Commons Attribution-NonCommercial 3.0 Unported Licence.

Table 2 Selected bond distances (Å) and angles (°) for the studied complexes **2–4**[a]

Distances	2	3	4	Angles	2	3	4	Torsion angles	2	3	4
Mn–N1	2.218(7)	2.2020(11)	2.195(6)	N1–Mn–N2	73.0(3)	72.15(4)	72.8(3)	N1–C–C–N2	−29.7	−22.0	−25.7
Mn–N2	2.274(7)	2.3040(11)	2.308(7)	N1–Mn–N3	72.3(3)	73.37(4)	72.3(3)	N2–C–C–O1	57.0	55.8	56.6
Mn–N3	2.292(8)	2.2953(11)	2.334(7)	N2–Mn–O1	72.8(3)	72.87(4)	72.2(3)	O1–C–C–O2	−56.0	−59.1	−54.8
Mn–O1	2.293(6)	2.3019(9)	2.294(6)	O2–Mn–N3	73.8(3)	73.32(4)	73.7(2)	O2–C–C–N3	58.1	59.0	61.4
Mn–O2	2.285(6)	2.3271(10)	2.310(6)	O2–Mn–O1	69.6(2)	70.57(3)	71.3(3)	N3–C–C–N1	−24.1	−33.0	−27.6
Mn–X_{ax}1	2.9493(14) I1A	2.2339(12)N4	2.238(7) N4A	X_{ax}1–Mn–X_{ax}2	178.80(5)	174.68(5)	176.7(3)				
Mn–X_{ax}2	3.0329(15) I2A	2.2293(12) N7	2.210(8) N5A								

[a] Entire list of bond distances and angles is available in Table S1 in the ESI.†

For **4**, the observed Mn–N–C angles are little bit higher in comparison with those found in [Mn(15-pydienN_3O_2)$(NCS)_2$] (126.1° and 130.4°).[6] On the other hand, the X–Mn–X angles (X represents the donor atom of the axial ligand) are close to the ideal linear arrangement (178.8°, 174.7° and 176.7° for **2**, **3** and **4**, respectively, Table 3).

In the crystal structure of all the compounds, an extensive system of N–H···X and C–$H_{aromatic}$···X hydrogen non-covalent contacts (X = I, N, or S atom of the axial ligand) as well as π–π stacking interactions were found. These non-covalent contacts and interactions strongly influenced the final crystal packing of the complexes (Table S2 in the ESI†) as well as the magnetic properties (see the sections of magnetic properties and DFT calculations). In the crystal structure of **2**, a zig-zag 1D chain is formed by two N–H···I hydrogen bonds between the two [Mn**L**I_2] units (Fig. 3). Furthermore, these infinite chains are connected to each other by two C–$H_{aromatic}$···I non-covalent contacts as well as by face-to-face π–π interactions (centroid···centroid distance = Cg···Cg = 3.758(1) Å), which all together form almost planar 2D sheets (layers) separated from each other (*i.e.* no non-covalent contacts observed).

The 1D chain motif can be also found in the crystal structures of **3** and **4**, where again the complex units are connected by N–H···N and N–H···S hydrogen bonds, respectively. In **3**, similarly as in **2**, this chain can be considered as a zig-zag, while it is almost linear in **4**. This trend can be clearly demonstrated by the values of the dihedral angle between the two MnN_3O_2 least-square planes in the chain which are 45.6°, 60.2°, and 8.4° for **2**, **3**, and **4**, respectively (Fig. 3). As for **2**, this angle of 45.6° is slightly higher than the 41.6° observed in [Mn**L**Cl_2].[5] Additionally, in the crystal structure of [Mn(15-pydienN_3O_2)$(NCS)_2$],[6] there are no NH groups and thus, only C–$H_{aromatic}$···S non-covalent contacts and π–π stacking are present, and thus, a completely different arrangement of the complex units was found in comparison with **4**.

On the other hand, the linking of these chains is different in **3** and **4**. In **3**, these 1D chains are linked by C–$H_{aromatic}$···N non-covalent contacts and face-to-face π–π interactions (Cg···Cg = 3.467(1) Å) forming zig-zag bent 2D sheets which are not connected to each other by any non-covalent contacts, whereas in **4**, these 1D chains are linked by C–$H_{aromatic}$···S non-covalent contacts and face-to-face π–π interactions (Cg···Cg = 3.698(1)

Table 3 Detailed description of the coordination sphere of Mn^{II} atoms in the molecular structures of complexes **2**, **3** and **4**

Complex	[Mn**L**I_2] (**2**)	[Mn**L**$(N_3)_2$] (**3**)	[Mn**L**$(NCS)_2$] (**4**)		
Illustration of the coordination sphere of Mn^{II}	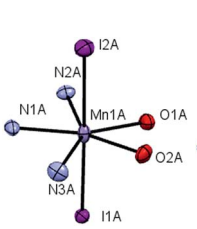	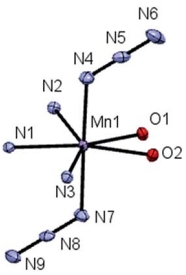	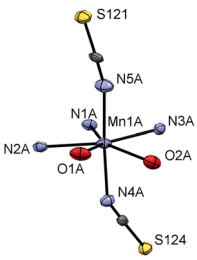	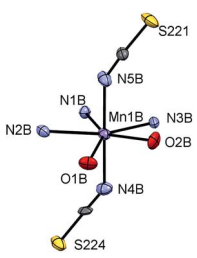	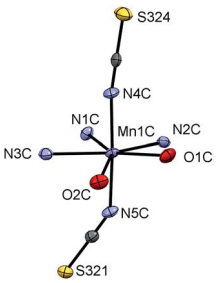
Metal–axial donor atom distance (Å)	I1A 2.9493(14) I2A 3.0329(15)	N4 2.2339(12) N7 2.2293(12)	N4A 2.238(7)[b] N5A 2.210(8)[b]	N4B 2.194(7)[b] N5B 2.202(8)[b]	N4C 2.200(7)[b] N5C 2.233(7)[b]
Angle (°)	—	119.6 121.2	145.7(7)[b] 165.0(8)[b]	141.1(8)[b] 142.9(8)[b]	165.1(8)[b] 149.1(7)[b]
Mn–N–N(S)	—		(Mn1A–N4A–C123)[b] (Mn1A–N5A–C120)[b]	(Mn1B–N4B–C223)[b] (Mn1B–N5B–C220)[b]	(Mn1C–N4C–C323)[b] (Mn1C–N5C–C320)[b]
Angle (°) X–Mn–X[a]	178.80(5), 177.25(5)[b]	174.68(5)	176.7(3)[b]	179.1(3)[b]	174.9(3)[b]

[a] X = axial donor atom. [b] Two and three crystallographically independent molecules in the asymmetric unit of **2** and **4**, respectively, were found.

Open Access Article. Published on 24 March 2016. Downloaded on 12/4/2025 5:50:39 AM.
This article is licensed under a Creative Commons Attribution-NonCommercial 3.0 Unported Licence.

Å) forming almost planar 2D sheets which are linked to each other by C–$H_{aromatic}$···S non-covalent contacts, thus giving rise to a supramolecular 3D network. Despite many crystallization attempts, single crystals of **1** and **5** suitable for X-ray diffraction analysis were not prepared. But nevertheless, at least a powder diffraction pattern for **1** was recorded (Fig. S3†) and it showed that **1** and **2** are isostructural.

IR spectroscopy

The vibration characteristics for the coordinated ligand **L** were present in the IR spectra of all the complexes (Fig. S4 in the ESI†), *i.e.* a strong broad signal at ~3230 cm^{-1} (stretching vibrations of the two NH groups), strong doublets at ~2900 cm^{-1} (stretching CH_2 vibrations), a medium sharp doublet at 1600 and 1575 cm^{-1}, and a medium broad signal(s) at ~1460 cm^{-1} (wagging vibrations of the pyridine ring). Furthermore, characteristic strong absorption bands at 2023, 2059 and 2123 cm^{-1} assigned to the asymmetric stretching vibrations of the N_3^- group in **3**, NCS^- group in **4**, and CN^- group in **5**, respectively, were observed. The position of this band in **4** was almost the same as that observed for $[Mn(15\text{-pydienN}_3O_2)(NCS)_2]$ (2058 cm^{-1})[6] or $[Mn(cyclam)(NCS)_2]^+$ (2060 cm^{-1}, cyclam = 1,4,8,11-tetraazacyclotetradecane).[31] The position of the broad absorption band of N_3^- in **3** was found at lower wavenumbers than in the case of the end-to-end μ-1,3-bridged azide between two Mn^{II} centres in $([Mn(15\text{-pydienN}_5)(N_3)]^+)_n$ (2049 cm^{-1})[10] as well as in the case of other azido complexes with manganese $[Mn(saldien)(N_3)]$ (2067 and 2056 cm^{-1}, saldien = *N*,*N*′-bis(salicylidene)diethylenetriamine)[32] or $[N(afa^{Cy})_3Mn(N_3)]$ (2067 cm^{-1}, $N(afa^{Cy})_3$ = tris(5-cycloaminoazafulvene-2-methyl)-amine).[33] On the other hand, the absorption band of the CN^- group in **5** corresponded to the bridging mode of its coordination, whose position was comparable with the 2113 cm^{-1} observed in $[Mn(15\text{-pydienN}_3O_2)(H_2O)]_2[Mn(CN)_6](ClO_4)\cdot 3H_2O$[34] and 2110 cm^{-1} observed in $[Mn(salen)(CN)]_n$[35] (H_2-salen = bis(salicylidene)-ethylenediamine). These findings together with the broad character of the signal[36] suggested the 1D chain polymeric structure of complex **5**.

TG/DTA analysis

The results of the simultaneous TG/DTA analyses in a dynamic air atmosphere are similar for complexes **1**, **2**, **4** and **5**. The data for the representative complex **4** are shown in the ESI in Fig. S5.† No weight loss was observed until a temperature of ~180 °C, showing the absence of any coordinated/uncoordinated solvent molecules. Above 180 °C (**1** and **5**) or 280 °C (**2** and **4**), the decomposition proceeded in two (**1**, **2** and **4**) or three (**5**) steps without formation of thermally stable intermediates and it was accompanied with a few exo-effects. The decomposition was completed above 600 °C, except for complex **4**, in which an additional weight loss of 5.0% occurred between 613 and 766 °C. The products of thermal decomposition were not studied in detail, but the remaining weight percentage corresponds with the formation of Mn_2O_3 (% found/calcd: 16.1/16.9, 14.7/14.1, 19.7/18.7 and 18.3/18.3 for **1**, **2**, **4**, and **5**, respectively).

Magnetic properties

For all the prepared Mn^{II} complexes **1–5**, temperature and field dependent magnetic data were acquired and they are depicted in Fig. 4 and S6–S10 (in the ESI†). The room temperature values of the effective magnetic moment (μ_{eff}) span the 5.9–6.1 μ_B interval, which means that they are close to the theoretical spin-only value for $S = 5/2$, equal to 5.9 μ_B ($g = 2.0$). On lowering the temperature, there is a drop of μ_{eff} below 30 K down to 5.3–5.9 μ_B at $T = 1.9$ K

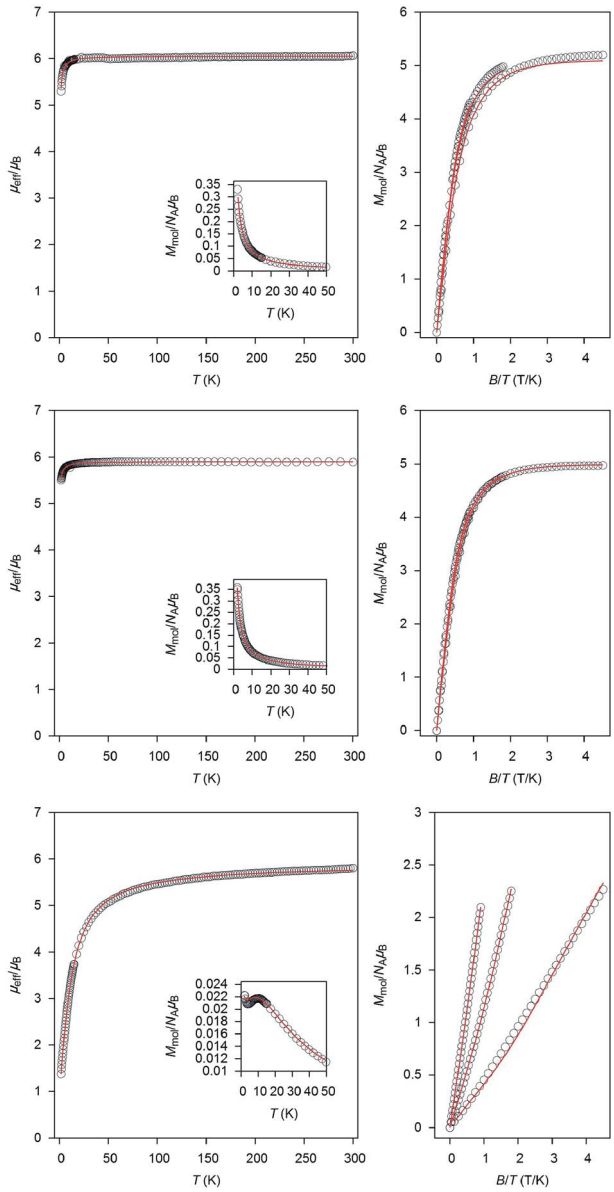

Fig. 4 Magnetic data for compounds **2** (top), **4** (middle) and **5** (bottom). Temperature dependence of the effective magnetic moment and molar magnetization measured at $B = 0.1$ T in the inset (left), and reduced isothermal magnetization measured at $T = 2$, 5 and 10 K (right). The empty circles represent the experimental data points and the full lines represent the best fits calculated with $D = -0.44(3)$ cm^{-1}, $g = 2.046(1)$, and $zj = -0.099(4)$ cm^{-1} for **2**, and $D = 0.12(4)$ cm^{-1}, $g = 1.996(1)$, and $zj = -0.066(1)$ cm^{-1} for **4** using eqn (1), and with $J = -1.72(1)$ cm^{-1}, $g = 1.992(2)$, and $x_{PI} = 1.3(1)$ % for **5** using eqn (6).

Open Access Article. Published on 24 March 2016. Downloaded on 12/4/2025 5:50:39 AM.
This article is licensed under a Creative Commons Attribution-NonCommercial 3.0 Unported Licence.

for **1–4**, which is most probably the result of weak intermolecular magnetic interactions mediated by non-covalent contacts (hydrogen bonds/π–π stacking) and also by the small magnetic anisotropy of Mn^{II} atoms in the heptacoordinated environment. In the case of **5**, the overall magnetic behaviour is different to **1–4**, the μ_{eff} is continuously decreasing from room temperature down to 1.37 μ_B at $T = 1.9$ K, and there is also a maximum of the M_{mol} *vs.* T curve at $T = 9.5$ K, which is a fingerprint of antiferromagnetic exchange either in a homo-spin dimer or uniformly coupled 1D chain. Moreover, the isothermal magnetization also significantly deviates from the Brillouin function. We can speculate that this is the result of the isotropic exchange mediated by the cyanido ligands in the bridging mode.

First, the magnetic data of **1–4** were treated with the spin Hamiltonian for a monomeric system

$$\hat{H}^{mono} = D(\hat{S}_z^{\,2} - \hat{S}^2/3) + \mu_B B g \hat{S}_a - zj\langle\hat{S}_a\rangle\hat{S}_a \quad (1)$$

where the single ion zero-field splitting parameter D, isotropic g-factor and molecular field correction zj parameters are present. $\langle S_a\rangle$ is a thermal average of the molecular spin projection in the a-direction of the magnetic field defined as $B_a = B(\sin\theta\cos\varphi, \sin\theta\sin\varphi, \cos\theta)$ with the help of the polar coordinates. Then, the molar magnetization in the a-direction of the magnetic field can be numerically calculated as:

$$M_a = -N_A \frac{\sum_i \left(\sum_k \sum_l C_{ik}^{\,+}(Z_a)_{kl} C_{li} \right) \exp(-\varepsilon_{a,i}/kT)}{\sum_i \exp(-\varepsilon_{a,i}/kT)} \quad (2)$$

where Z_a is the matrix element of the Zeeman term for the a-direction of the magnetic field and C is the eigenvectors resulting from the diagonalization of the complete spin Hamiltonian matrix. The inclusion of zj means that an iterative procedure was applied.[37] Then, the averaged molar magnetization of the powder sample was calculated as an integral (orientational) average:

$$M_{mol} = 1/4\pi \int_0^{2\pi} \int_0^{\pi} M_a \sin\theta \mathrm{d}\theta \mathrm{d}\varphi \quad (3)$$

We also tested both signs of the D parameter during fitting procedures and the results are summarized in Table 4. It is evident that similarly good fits were obtained for both signs of D. The largest magnetic anisotropy, $|D|$, was found in complex **1** ($D = 0.67(7)$ cm^{-1} or $D = -0.55(5)$ cm^{-1}), while a negligible D parameter was found in **3** ($D = 0$). Moreover, non-negligible magnetic intermolecular interactions seem to be present in compounds **1**, **2** and **3**, where $zj \approx -0.1$ cm^{-1} and slightly weaker interactions were found in **4** ($zj \approx -0.07$ cm^{-1}). Moreover, it must be stressed that we also tried to fit experimental data with simplified models, either by neglecting ZFS (D) or the molecular field correction (zj), but these models were unable to properly describe simultaneously both the temperature and field dependent magnetic data of **1**, **2** and **4**.

In the case of compound **5**, where the exact structural motif is unknown, the two spin Hamiltonian models were tested. First, the experimental data were treated with the dinuclear spin Hamiltonian (H^{dimer}):

$$\hat{H}^{dimer} = -J\left(\vec{S}_1 \cdot \vec{S}_2\right) + \sum_{i=1}^{2} D_i\left(\hat{S}_{i,z}^{\,2} - \hat{S}_i^{\,2}/3\right) + \mu_B B g_i \hat{S}_a \quad (4)$$

where the first term describes the isotropic exchange between paramagnetic manganese(II) atoms within the dimer and the rest of the terms were already explained. Now, the molar magnetization in the a-direction of the magnetic field was calculated as:

$$M_a = N_A kT \frac{\mathrm{d}\ln Z}{\mathrm{d}B} \quad (5)$$

where Z is the partition function and again the integral average was calculated using eqn (3). In this case, the best fit was obtained only for the positive D parameter, which resulted in $J = -2.79(4)$ cm^{-1}, $D = 0.6(3)$ cm^{-1}, $g = 1.978(3)$, and $x_{PI} = 2.2(2)$% (Fig. S10†), where also the monomeric paramagnetic impurity (PI) was included in order to describe a low temperature increase of the mean susceptibility. A second model attempts to mimic the 1D uniformly coupled spin chain by a finite-sized closed ring with the following spin Hamiltonian (H^{1D}):

$$\hat{H}^{1D} = -J\left(\vec{S}_1 \cdot \vec{S}_N\right) - J\sum_{i=1}^{N-1}\left(\vec{S}_1 \cdot \vec{S}_{i+1}\right) + \sum_{i=1}^{N} \mu_B B g_i \hat{S}_z \quad (6)$$

The number of centres was set to seven ($N = 7$), which resulted in already 279 936 magnetic levels. In order to be able to deal with such a large system, the zero-field term was neglected and then the coupled basis set could be utilized, which significantly simplifies the calculation of the magnetic properties.[39] The advantage of this procedure is that both the temperature and field dependent data can be fitted simultaneously. As a result, these parameters were obtained: $J = -1.72(1)$ cm^{-1}, $g = 1.992(2)$,

Table 4 The spin Hamiltonian parameters (eqn (1)) for **1–4**[a]

Complex	**1**	**2**	**3**	**4**
$D > 0$	$g = 2.035(2)$	$g = 2.046(1)$		$g = 1.996(1)$
	$D = 0.67(7)$	$D = 0.45(5)$	$g = 2.054(2)$	$D = 0.12(4)$
	$zj = -0.109(7)$	$zj = -0.099(4)$	$D = 0$	$zj = -0.066(1)$
$D < 0$	$g = 2.034(2)$	$g = 2.046(1)$	$zj = -0.099(5)$	$g = 1.996(1)$
	$D = -0.55(5)$	$D = -0.44(3)$		$D = -0.11(4)$
	$zj = -0.104(7)$	$zj = -0.099(4)$		$zj = -0.066(6)$

[a] Values of D and zj parameters are in cm^{-1}.[38]

Open Access Article. Published on 24 March 2016. Downloaded on 12/4/2025 5:50:39 AM.
This article is licensed under a Creative Commons Attribution-NonCommercial 3.0 Unported Licence.

and x_{PI} = 1.3(1)% (Fig. 4). As far as we know, Mn^{II}–CN–Mn^{II} systems are very rare, because usually one or both Mn atoms are in the oxidation state +III. One described example is a Mn^{II} complex with 1,4-bis(2-pyridylmethyl)-1,4,7-triazacyclononane (dmptacn) $[\{Mn(dmptacn)\}_2CN](ClO_4)_3$ for which only the negative value of the Weiss constant, $\theta = -0.31$ K,[40] was observed, as well as in some Mn^{II} Prussian blue analogues.[41,42]

DFT calculations

The analysis of the experimental magnetic data revealed weak magnetic interactions among Mn^{II} atoms in the solid state. With the aim to continue in our effort in recognizing/characterizing efficient magnetic exchange pathways mediated by non-covalent contacts,[5,43] we performed theoretical calculations of the isotropic exchange parameter J in selected molecular fragments based on the X-ray structures of **2–4**. Both the interactions within supramolecular 1D chains visualized in Fig. 3 and interchain interactions (shown in the ESI in Table S3†) were calculated using the B3LYP functional together with the def2-TZVP(-f) basis set utilizing the ORCA computational package. The values of J parameters were calculated by two approaches, either using Ruiz's formula:[44]

$$J^{Ruiz} = 2\Delta/[(S_1 + S_2)(S_1 + S_2 + 1)] \quad (7)$$

or Yamaguchi's formula:[45]

$$J^{Yam} = 2\Delta/[\langle S^2\rangle_{HS} - \langle S^2\rangle_{BS}] \quad (8)$$

where Δ is the energy difference between the broken symmetry spin state (BS) and high-spin state (HS):

$$\Delta = E_{BS} - E_{HS} \quad (9)$$

using this form of the spin Hamiltonian for the dinuclear system:

$$\hat{H} = -J(\vec{S}_1 \cdot \vec{S}_2) \quad (10)$$

The resulting J values are listed in Table 5. It is evident that in the crystal structure of **2**, the strength of the intrachain and interchain antiferromagnetic interactions is almost equal. In contrast, in **3**, there is the strongest antiferromagnetic exchange within the supramolecular chain among compounds **2–4**, and negligible interchain interaction. A similar situation is found in **4**, where again intrachain interaction is pronounced. Furthermore, apparently the strength of antiferromagnetic exchange is not a simple function of the metal–metal distance (Table 5), so it is obvious that the utilization of theoretical methods is an inevitable tool for better understanding of magnetic interactions in the solid state.

Table 5 The calculated J parameters for selected dinuclear molecular fragments of **2–4** using B3LYP/def2-TZVP(-f)[a]

Complex	2	3	4	4	4
Intrachain					
d(Mn···Mn) (Å)	7.337	7.655	7.880	8.024	8.499
Δ (cm^{-1})	−0.335	−1.476	−0.413	−0.348	−0.653
J^R (cm^{-1})	−0.022	−0.099	−0.028	−0.023	−0.044
J^Y (cm^{-1})	−0.027	−0.12	−0.033	−0.028	−0.052
Interchain					
d(Mn···Mn) (Å)	7.729	6.947	6.918		
Δ (cm^{-1})	−0.348	+0.002	+0.023		
J^R (cm^{-1})	−0.023	0.0	+0.002		
J^Y (cm^{-1})	−0.028	0.0	+0.002		

[a] The respective molecular fragments are shown in the ESI in Table S3.†

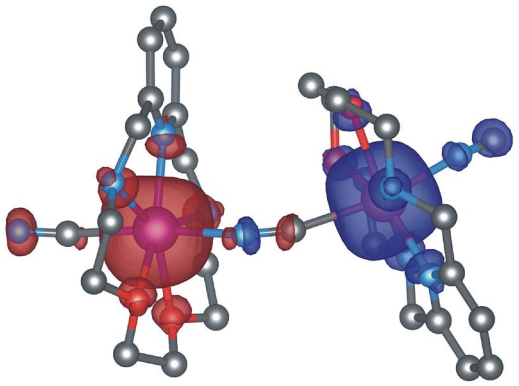

Fig. 5 The DFT optimized geometry of the $[(CN)LMn(\mu\text{-}CN)MnL(CN)]^+$ molecular fragment of **5** and calculated isodensity surfaces of the broken symmetry spin states plotted with the cut-off values of 0.003 ea_0^{-3}. Positive and negative spin densities are represented by dark blue and dark red surfaces, respectively. Selected bond lengths (Å): Mn–N_{py} = 2.228/2.251, Mn–N_H = 2.346/2.337/2.350/2.352, and Mn–O = 2.327/2.469/2.358/2.332. Hydrogen atoms are omitted for clarity.

Furthermore, we also tried to support our presumption that in the case of compound **5**, a polymeric structure of $\{[MnL(\mu\text{-}CN)](ClO_4)\}_n$ is formed, in which cyanide anions act as bridging ligands. Therefore, the dinuclear molecular fragment of $[(CN)LMn(\mu\text{-}CN)MnL(CN)]^+$ was constructed and its geometry optimized at the B3LYP/def2-TZVP(-f) level of theory (Fig. 5). The metal–donor atom distances were found to be similar to those determined in the X-ray structures of **2–4**. Afterwards, the J parameters were calculated for this fragment, which resulted in $J^R/J^Y = -2.54/-3.06$ cm^{-1}. These values are in good agreement with $J = -2.79$ cm^{-1} determined from the experimental magnetic data using the spin Hamiltonian for a dinuclear system. Thus, this finding indirectly supports the formation of a polymeric species, where dominant magnetic exchange is mediated by the cyanido bridging ligands.

Conclusions

A series of heptacoordinated Mn^{II} complexes **1–5** containing a pentadentate 15-membered pyridine-based macrocycle **L** and two axial coligands with different coordination abilities (Br^-, I^-, N_3^-, NCS^- or CN^-) was prepared and thoroughly characterized. The pentagonal-bipyramidal coordination sphere of Mn^{II} was axially elongated (in **2**) or compressed (in **3** and **4**) depending on the type of coligand. Based on an analysis of structural and magnetic data for **1–4**, the single ion magnetic anisotropy of

Open Access Article. Published on 24 March 2016. Downloaded on 12/4/2025 5:50:39 AM.
This article is licensed under a Creative Commons Attribution-NonCommercial 3.0 Unported Licence.

Mn^{II} with a $3d^5$ configuration in the pentagonal-bipyramidal coordination environment is very small ($|D| < 0.7$ cm^{-1}), which prevented us from drawing a quantitative conclusion about the impact of the axial coligands on *D*. Therefore no magneto-structural correlation could be carried out reliably in contrast to other studies on complexes with different metal ions or different coordination geometries. On the other hand, the magnetic nature of **1–4** was more markedly influenced by noticeable non-covalent contacts, which are responsible for the 1D chain supramolecular crystal structures of the complexes. Moreover, the performed DFT calculations supported the experimental results and identified that the weak antiferromagnetic exchange in **3** and **4** was exclusively mediated *via* intrachain hydrogen bonds, while it was equally mediated by intrachain as well as interchain hydrogen bonds in **2**. In addition to this, the calculations showed that the Mn···Mn distance cannot be considered as the main criterion for the prediction of the intensity of the magnetic exchange. The polymeric character of **5** was suggested by fitting the magnetic data with a dimeric/polymeric model providing a weak antiferromagnetic exchange coupling, which was subsequently supported by DFT calculations based on the theoretically optimized structure of the dimeric fragment $[(CN)\mathbf{L}Mn(\mu\text{-}CN)Mn\mathbf{L}(CN)]^+$ as well. To conclude, this is the first attempt to correlate the structure of Mn^{II} heptacoordinated complexes with their magnetic properties. It is evident that the magnetic anisotropy is little affected by the axial ligands within the pentacoordinate bipyramidal chromophore, but the presented $[Mn\mathbf{L}]^{2+}$ fragment can be successfully employed as a high-spin ($S = 5/2$) building block for the synthesis of structurally more complex polymeric species with eventually more interesting magnetic properties.

Acknowledgements

The authors gratefully thank the Czech Science Foundation (A Grant No. 13-32167P) and the National Program of Sustainability (NPU LO1305) of the Ministry of Education, Youth, and Sports of the Czech Republic for the financial support. X-ray diffraction experiments of complexes **2** and **4** were realized in the X-ray Diffraction and BioSAXS Core Facility of CEITEC (Central European Institute of Technology) under CEITEC-open access project, ID number LM2011020, funded by the Ministry of Education, Youth and Sports of the Czech Republic under the activity, "Projects of major infrastructures for research, development and innovations". In this context, the authors also wish to thank Assoc. Prof. Jaromír Marek for the X-ray diffraction measurements and data reduction regarding complexes **2** and **4**.

Notes and references

1 M. Rezaeivala and H. Keypour, *Coord. Chem. Rev.*, 2014, **280**, 203–253.
2 E. L. Gavey and M. Pilkington, *Coord. Chem. Rev.*, 2015, **296**, 125–152.
3 J. S. Miller and D. Gatteschi, Molecule-based magnets themed issue No. 6, *Chem. Soc. Rev.*, 2011, **40**, 3053–3368.
4 B. Drahoš, J. Kotek, P. Hermann, I. Lukeš and E. Tóth, *Inorg. Chem.*, 2010, **49**, 3224–3238.
5 B. Drahoš, R. Herchel and Z. Trávníček, *Inorg. Chem.*, 2015, **54**, 3352–3369.
6 M. G. B. Drew, A. H. bin Othman, S. G. McFall, P. D. A. Mcllroy and S. M. Nelson, *Dalton Trans.*, 1977, **12**, 1173–1180.
7 D. Zhang, H. Wang, L. Tian, J. Jiang and Z.-H. Ni, *CrystEngComm*, 2009, **11**, 2447–2451.
8 F. Bonadio, M.-C. Senna, J. Ensling, A. Sieber, A. Neels, H. Stoeckli-Evans and S. Decurtins, *Inorg. Chem.*, 2005, **44**, 969–978.
9 C. Paraschiv, M. Andruh, Y. Journaux, Z. Žak, N. Kyritsakas and L. Ricard, *J. Mater. Chem.*, 2006, **16**, 2660–2668.
10 K. A. Sra, J.-P. Sutter, P. Guionneau, D. Chasseau, J. V. Yakhmi and O. Kahn, *Inorg. Chim. Acta*, 2000, **300–302**, 778–782.
11 C. Paraschiv, J.-P. Sutter, M. Schmidtmann, A. Müller and M. Andruh, *Polyhedron*, 2003, **22**, 1611–1615.
12 J. Wang, B. Slater, A. Alberola, H. Stoeckli-Evans, F. S. Razavi and M. Pilkington, *Inorg. Chem.*, 2007, **46**, 4763–4765.
13 K. S. Murray and C. J. Kepert, *Top. Curr. Chem.*, Springer, 2004, vol. 233–235.
14 I. Nemec, R. Herchel, R. Boca, Z. Travnicek, I. Svoboda, H. Fuess and W. Linert, *Dalton Trans.*, 2011, **40**, 10090–10099.
15 C. Krüger, P. Augustín, I. Nemec, Z. Trávníček, H. Oshio, R. Boča and F. Renz, *Eur. J. Inorg. Chem.*, 2013, **2013**, 902–915.
16 P. Masárová, P. Zoufalý, J. Moncoľ, I. Nemec, J. Pavlik, M. Gembický, Z. Trávníček, R. Boča and I. Šalitroš, *New J. Chem.*, 2015, **39**, 508–551.
17 G. A. Craig and M. Murrie, *Chem. Soc. Rev.*, 2015, **44**, 2135–2147.
18 S. E. Stavretis, M. Atanasov, A. A. Podlesnyak, S. C. Hunter, F. Neese and Z.-L. Xue, *Inorg. Chem.*, 2015, **54**, 9790–9801.
19 S. Mossin, B. L. Tran, D. Adhikari, M. Pink, F. W. Heinemann, J. Sutter, R. K. Szilagyi, K. Meyer and D. J. Mindiola, *J. Am. Chem. Soc.*, 2012, **134**, 13651–13661.
20 W. Kabash, XDS, *Acta Crystallogr., Sect. D: Biol. Crystallogr.*, 2010, **66**, 125–132.
21 Bruker, *Apex3*, Bruker AXS Inc., Madison, Wisconsin, USA, 2015.
22 G. M. Sheldrick, *Acta Crystallogr., Sect. C: Struct. Chem.*, 2015, **71**, 3–8.
23 C. F. Macrae, I. J. Bruno, J. A. Chisholm, P. R. Edgington, P. McCabe, E. Pidcock, L. Rodriguez-Monge, R. Taylor, J. van de Streek and P. A. Wood, *J. Appl. Crystallogr.*, 2008, **41**, 466–470.
24 F. Neese, *WIREs Computational Molecular Science*, 2012, **2**, 73–78.
25 F. Neese, *Coord. Chem. Rev.*, 2009, **253**, 526–563.
26 C. Lee, W. Yang and R. G. Parr, *Phys. Rev. B: Condens. Matter Mater. Phys.*, 1988, **37**, 785–789; A. D. Becke, *J. Chem. Phys.*, 1993, **98**, 1372–1377; A. D. Becke, *J. Chem. Phys.*, 1993, **98**, 5648–5652; P. J. Stephens, F. J. Devlin, C. F. Chabalowski and M. J. Frisch, *J. Phys. Chem.*, 1994, **98**, 11623–11627.

Open Access Article. Published on 24 March 2016. Downloaded on 12/4/2025 5:50:39 AM.
This article is licensed under a Creative Commons Attribution-NonCommercial 3.0 Unported Licence.

27 A. Schafer, H. Horn and R. Ahlrichs, *J. Chem. Phys.*, 1992, **97**, 2571–2577; A. Schafer, C. Huber and R. Ahlrichs, *J. Chem. Phys.*, 1994, **100**, 5829–5835; F. Weigend and R. Ahlrichs, *Phys. Chem. Chem. Phys.*, 2005, **7**, 3297–3305.
28 F. Neese, F. Wennmohs, A. Hansen and U. Becker, *Chem. Phys.*, 2009, **356**, 98–109; R. Izsak and F. Neese, *J. Chem. Phys.*, 2011, **135**, 144105.
29 S. Grimme, J. Antony, S. Ehrlich and H. Krieg, *J. Chem. Phys.*, 2010, **132**, 154104; S. Grimme, S. Ehrlich and L. Goerigk, *J. Comput. Chem.*, 2011, **32**, 1456–1465.
30 K. Momma and F. Izumi, *J. Appl. Crystallogr.*, 2011, **44**, 1272–1276.
31 P.-K. Chan and C.-K. Poon, *J. Chem. Soc., Dalton Trans.*, 1976, 858–862.
32 S. Alavi, H. Hosseini-Monfareda and M. Siczekba, *J. Mol. Catal. A: Chem.*, 2013, **377**, 16–28.
33 E. M. Matson, Y. J. Park, J. A. Bertke and A. R. Fout, *Dalton Trans.*, 2015, **44**, 10377–10384.
34 S. L. Zhang, X. H. Zhao and X. Y. Wang, *Dalton Trans.*, 2015, **44**, 15189–15197.
35 N. Matsumoto, Y. Sunatsuki, H. Miyasaka, Y. Hashimoto, D. Luneau and J.-P. Tuchagues, *Angew. Chem., Int. Ed.*, 1999, **38**, 171–173.
36 Z. Trávníček, R. Zbořil, M. Matiková-Maľarová, B. Drahoš and J. Černák, *Chem. Cent. J.*, 2013, **7**, 28.
37 R. Boča, *Theoretical Foundations of Molecular Magnetism*, Elsevier, Amsterdam, 1999.
38 The standard deviations were calculated as $\sigma_i = (\mathrm{P}_{ii}^{-1}S/(N-k))^{-1/2}$, where $P_{ij} = \Sigma(\delta\mu_n/\delta a_i \delta\mu_n/\delta a_j)$ and $S = \Sigma(\mu_n - \mu_n^{\mathrm{exp}})^2$ with $n = 1$ to N; a_i and a_j are fitted parameters, N is the number of experimental points (sum of temperature and field dependent data), and μ_n and μ_n^{exp} are the calculated and experimental effective magnetic moments for a given temperature and magnetic field. σ_i was then multiplied by Student's $t_{95\%}$ to provide confidence limits with 95% probabilities listed in the text.
39 R. Herchel, Z. Šindelář, Z. Trávníček, R. Zbořil and J. Vančo, *Dalton Trans.*, 2009, 9870–9880.
40 R. J. Parker, L. Spiccia, B. Moubaraki, K. S. Murray, D. C. R. Hockless, A. D. Rae and A. C. Willis, *Inorg. Chem.*, 2002, **41**, 2489–2495.
41 J.-H. Her, P. W. Stephens, C. M. Kareis, J. G. Moore, K. S. Min, J.-W. Park, G. Bali, B. S. Kennon and J. S. Miller, *Inorg. Chem.*, 2010, **49**, 1524–1534.
42 C. M. Kareis, S. H. Lapidus, J.-H. Her, P. W. Stephens and J. S. Miller, *J. Am. Chem. Soc.*, 2012, **134**, 2246–2254.
43 R. Herchel, I. Nemec, M. Machata and Z. Trávníček, *Inorg. Chem.*, 2015, **54**, 8625–8638; I. Nemec, R. Herchel, T. Šilha and Z. Trávníček, *Dalton Trans.*, 2014, **43**, 15602–15616.
44 E. Ruiz, J. Cano, S. Alvarez and P. Alemany, *J. Comput. Chem.*, 1999, **20**, 1391–1400; E. Ruiz, A. Rodríguez-Fortea, J. Cano, S. Alvarez and P. Alemany, *J. Comput. Chem.*, 2003, **24**, 982–989.
45 K. Yamaguchi, Y. Takahara and T. Fueno, in *Applied Quantum Chemistry*, ed. V. H. Smith, Reidel, Dordrecht, 1986, p. 155; T. Soda, Y. Kitagawa, T. Onishi, Y. Takano, Y. Shigeta, H. Nagao, Y. Yoshioka and K. Yamaguchi, *Chem. Phys. Lett.*, 2000, **319**, 223.

 This journal is © The Royal Society of Chemistry 2016